Available online at www.sciencedirect.com
ScienceDirect
International Journal of Thermal Sciences 48 (2009) 174–187
International Journal of Thermal Sciences
www.elsevier.com/locate/ijts

Heat transfer of rotating rectangular duct with compound scaled roughness and V-ribs at high rotation numbers

Shyy Woei Chang [a,*], Tsun Lirng Yang [b], Tong-Miin Liou [c], Guo Fang Hong [b]

[a] *Thermal Fluids Laboratory, Department of Marine Engineering, National Kaohsiung Marine University, No. 142, Haijhuan Rd., Nanzih District, Kaohsiung, Taiwan, ROC*

[b] *Department of Marine Engineering, National Kaohsiung Marine University, No. 142, Haijhuan Rd., Nanzih District, Kaohsiung, Taiwan, ROC*

[c] *Department of Power Mechanical Engineering, National Tsing Hua University, Hsinchu, Taiwan, ROC*

Received 9 August 2007; received in revised form 1 March 2008; accepted 3 March 2008

Available online 3 April 2008

Abstract

Local heat transfer measurements for a radially rotating rectangular channel fitted with the compound roughness of staggered V-ribs and deepened scales on two opposite wide walls are performed at the parametric conditions of $10000 \leqslant Re \leqslant 24000$, $0 \leqslant Ro \leqslant 1$ and $0.137 \leqslant \Delta\rho/\rho \leqslant 0.274$. Heat transfer augmentations achieved by using this compound surface roughness at selected locations along the span and centerline of the leading and trailing walls of the rotating duct are 2.8–5 and 5–7.8 times of the Dittus–Boelter values respectively. No previous attempt has examined the heat transfer performances for such compound surface roughness in the rotating channel with cooling applications to gas turbine rotor blades. A selection of experimental data illustrates the HTE effectiveness with the individual and interdependent *Re, Ro* and buoyancy number (*Bu*) effects on heat transfer revealed. Empirical equations that calculate the averaged Nusselt numbers (*Nu*) over leading and trailing surfaces in the periodically developed flow region are derived to correlate all the heat transfer data generated by present study and permit the evaluation of interdependent and individual effects of *Re, Ro* and *Bu* on heat transfer.

Keywords: Turbine rotor blade; V-ribs and scaled roughness; High rotating number

1. Introduction

Modern gas turbine engines operate at turbine entry temperatures (TET) of about 1800–2000 K that are far above than the melting points of blade materials. With the large mechanical loads acting upon a turbine rotor blade under the harsh thermal environments, it is essential to incorporate complex internal cooling passages inside a rotor blade in order to assure its structural integrity and life span. But the consumption of coolant flow bled from the compressor into the rotor blade offsets the thermodynamic gains by operating the engine at such high TET. The research goal of improving heat transfer rates with the coolant consumption reduced for the cooling network inside turbine blades is therefore under constant pursuits. These pursuits call for a variety of passive HTE methods to be tested under rotating conditions [1–13]. The complex turbulent flows and heat transfer physics relative to these HTE measures for the rotating passages [1–13] are the primary concerns of both industrial and academic researchers. But the harsh thermal environment and the extremely high rotational speeds of rotor blades prohibit the fast progress in the experimental studies with the full coverage of engine conditions. It is particularly scarce of detailed flow measurements for these enhanced rotating passages at the realistic engine conditions. Nevertheless, having considered the suitability as parts of the cooling channels inside a rotor blade, several selective HTE measures are tested at the non-rotating conditions prior to performing the rotating tests. In this respect, the applicable HTE measures include surface ribs [14–18], dimples [19,20], pin-fins [21,22] and the scaled roughness [23]. Their thermal performances with the associated HTE mechanics are revealed through the non-rotating tests [14–23]. With rotation, the local HTE effectiveness attributed from these HTE measures is either amplified or

* Corresponding author.
E-mail address: swchang@mail.nkmu.edu.tw (S.W. Chang).

1290-0729/$ – see front matter
doi:10.1016/j.ijthermalsci.2008.03.001

Nomenclature

A, n	coefficient
AR	channel cross-sectional aspect ratio $= (W/H)$
Bu	buoyancy number $= Ro^2\beta(T_w - T_b)(R/d)$
D	diameter of scale ..... m
d	hydraulic diameter of the rectangular test channel ..... m
e^r	height of rib ..... m
e^s	depth of scale ..... m
H	channel height ..... m
k_f	thermal conductivity of fluid ..... $\mathrm{W\,m^{-1}\,K^{-1}}$
L	channel length ..... m
l^R	rib land ..... m
Nu	local Nusselt number $= qd/k_f(T_w - T_b)$
$\overline{Nu}$	averaged Nu at mid-rib location for periodically developed flow
Nu_0	local Nusselt number at zero rotational speed
Nu_∞	Nusselt number value evaluated from Dittus–Boelter correlation
P^r	pitch of rib ..... m
P^s	pitch of scale ..... m
Pr	Prandtl number $= \mu C_p/k$
q	convective heat flux ..... $\mathrm{W\,m^{-2}}$
R	rotating radius at mid-span of test duct from rotating axis ..... m
Re	Reynolds number $= \rho W_m d/\mu$
Ro	rotating number $= \Omega d/W_m$
T_b	fluid bulk temperature ..... K
T_w	wall temperature ..... K
W	channel width ..... m
W_m	mean flow velocity ..... $\mathrm{m\,s^{-1}}$
x	axial location referred to flow entry as origin ... m
X	dimensionless axial location (x/d)

Greek symbols

α	attack angle of V rib (degree)
β	thermal expansion coefficient of fluid ..... $\mathrm{K^{-1}}$
γ	attack angle of deepened scale (degree)
ρ	density of fluid ..... $\mathrm{kg\,m^{-3}}$
μ	fluid dynamic viscosity ..... $\mathrm{kg\,m^{-1}\,s^{-1}}$
Ω	rotational speed of test duct ..... $\mathrm{rad\,s^{-1}}$
Ψ, ϕ_1, ϕ_2	unknown functions

Subscripts

L	refers to centerline of rotating leading wall
T	refers to centerline of rotating trailing wall
0	refers to non-rotating situation

moderated due to the interdependent effects of Coriolis forces and rotating buoyancy. Here, these rotation induced heat transfer impacts vary with the shape and orientation of the rotating channel, the configurations of surface roughness, the connecting turns and the heating conditions [1–13]; while the mechanisms for HTE performances due to ribs, dimples or pin-fins are generally retained as those in the non-rotating channels.

A variety of surface ribs [14–18], dimples [19,20], pin-fins [21,22] and the scaled roughness [23] has been initially devised to enhance heat transfer rates in non-rotating ducts. These HTE measures [14–23] generally elevate turbulent heat transfer rates in a non-rotating channel as much as 200–450% of the Dittus–Boelter levels (Nu_∞) [24]. The rib-induced HTE mechanisms include the periodical penetration of protruding ribs across boundary layers, flow reattachments, turbulence promotions and the generation of cross-plane secondary flows by angled ribs. These various types of surface ribs [14–18] produce heat transfer augmentations in the range of 2–3.5 times of the Nu_∞ references in the non-rotating channels. With rotation, the Coriolis vortices interact with the rib-induced secondary flows that result in rich structures of cross-sectional secondary flows and therefore the various heat transfer performances. Variations of the channel orientation, the shape of rotating channel or the radial direction of the coolant flow alter the strength, structure and/or the direction of Coriolis secondary flows. Even with the agitated rib-flows in the rotating ribbed channels, the turbulence activities are promoted and suppressed over the unstable and stable walls respectively [25]. But rotating buoyancy effects are considerably suppressed from the scenarios found in the smooth-walled rotating channel due to the presence of surface ribs [26].

In the channel roughened by deepened dimples, the flow structures over the dimpled surface are characterized by vortex pairs those periodically shed from each dimple [19]. Local heat transfer enhancements are more pronounced near the downstream rim of each dimple. Averaged Nusselt numbers in a non-rotating dimpled channel fall between 1.85 and 2.89 times of the smooth walled channel [19]. Unlike the secondary flows induced by angled ribs, the strong and continuous vortical cells can not be established over the cross-section of a dimpled channel at the non-rotating condition. Vortical interactions between the Coriolis vortices and the rib-flows are absent in the rotating dimpled channel; but the Coriolis secondary flows sweep away the three-dimensional vortices triggered by dimples; and turbulences are promoted and suppressed over the unstable and stable walls, respectively. These Coriolis effects produce typical heat transfer enhancements and impediments over the unstable and stable dimpled walls. Local Nusselt numbers over the unstable and stable walls are respectively increased and reduced to the levels about 2.2–3.4 and 1.2–1.7 times of Nu_∞ references at the parametric conditions of $0.01 \leqslant Ro \leqslant 0.3$ [9].

Channels fitted with pin-fin array are widely adopted as a part of cooling network at the trailing edge of a rotor blade where the higher HTE effectiveness is required. Two primary vortex pairs downstream of each pin row, as the remnants of the two legs of horseshoe vortices, are formed by the blockage and streamline displacement effects. Even with the adiabatic pin-fin array that rules out the additional fin effects, the HTE

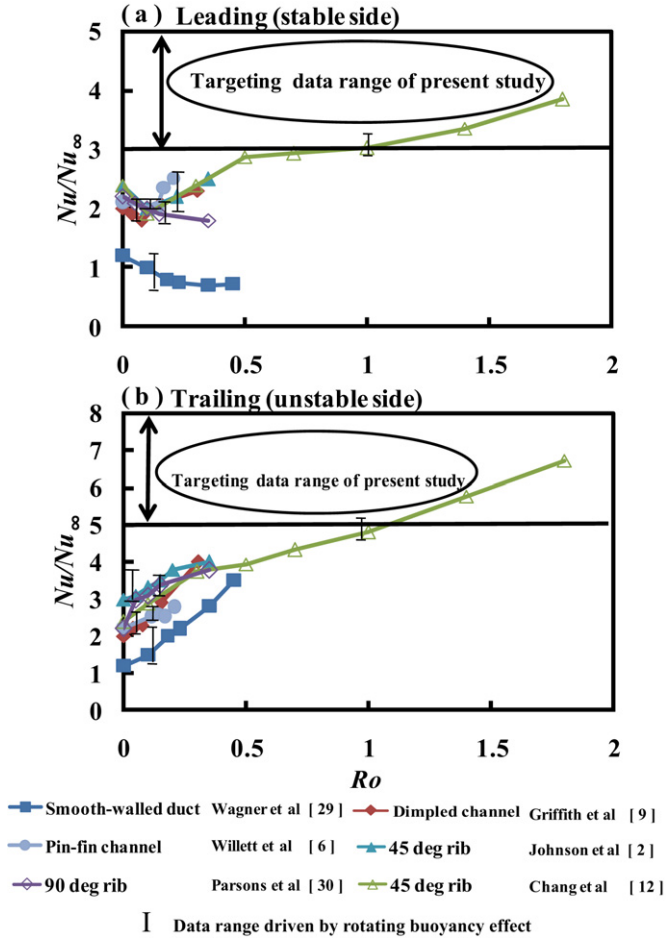

Fig. 1. Comparison of Nu/Nu_∞ performances for rotating ribbed, dimpled and pin-fin channels.

ratios for a non-rotating pin-fin channel fall in the range of 2–4 times of Nu_∞ [6,22,23]. When the pin-fin channel rotates, the pin-fin array that penetrates across the rotating channel considerably disturbs the development of cross-sectional Coriolis secondary flows. The typical vortical flow structures dominated by the downstream convection of the Coriolis secondary flows, as those developed in the rotating ribbed and dimpled channels are unlikely followed by the rotating pin-fin channel. But the mechanisms of flow instability due to the spanwise pressure gradients induced by Coriolis forces still prevail over the rotating pin-fin channel that interact with the disturbed Coriolis vortices to generate the peripheral heat transfer variations. Heat transfer levels over the stable and unstable walls of a rotating pin-fin channel are respectively raised and reduced to about 1.2–1.4 and 0.7–0.75 times of the non-rotating levels with $0.1 \leqslant Ro \leqslant 0.2$ [6]. Due to the limited heat transfer data available in the literature [6], the impacts of rotating buoyancy on heat transfer for the rotating pin-fin channel are not yet clear.

Fig. 1 summarizes heat transfer measurements in the rotating ribbed, dimpled and pin-fin channels on the (a) stable and (b) unstable walls in the form of Nu/Nu_∞ versus Ro. Along the stable wall (see Fig. 1(a)), the Nu/Nu_∞ ratio is initially reduced from the non-rotating level to a minimum value after which the subsequent heat transfer recovery is followed that can lead to the heat transfer improvements from the non-rotating references at high Ro. As Ro increases, the Nu/Nu_∞ ratios are consistently elevated from the non-rotating references along the unstable wall (see Fig. 1(b)). These data trends revealed in Fig. 1 feature the typically heat transfer performances in rotating channels which mainly characterize the Coriolis force effects. Data ranges covered by most of the rotating heat transfer tests are limited within $Ro \leqslant 0.5$ that are far less than the full coverage of the realistic engine conditions. For the purpose of validation, the previous heat transfer data for a rotating square duct fitted with staggered skew ribs reported by this research group [12] is compared with the data of Johnson et al. [2] as seen in Fig. 1. The favorable agreements between these two research groups on both stable and unstable walls in the data range of $0 \leqslant Ro < 0.5$ are observed. A detailed description for validating the heat transfer data generated by this research group for the static and rotating rib-roughened channels was reported in [12]. Also noticed in Fig. 1 at each Ro examined, the data bars for some data points available in the literature represent the range of buoyancy effects on heat transfer. By way of varying the surface roughness from ribs, dimples to pin-fins, the degrees of heat transfer variations from the non-rotating conditions are accordingly modified. Justified by the different degrees of heat transfer variations from the non-rotating references between these comparative groups collected in Fig. 1, the rotating ribbed and dimpled channels are the subjects of the larger Coriolis-force effects while the rotating pin-fin channel shows the weakest Ro effects. The Nu/Nu_∞ ratios for the rotating ribbed, dimpled and pin-fin channels are in the ranges of 2.4–6.7, 2–4, and 2.1–2.7, respectively.

The search for enhanced rotating surfaces those are compatible with the available manufacturing techniques for rotor blades has driven this research group looking into the present compound HTE measures. In order to provide a basic HTE element for the compound HTE measures, the scale-roughened HTE surface has been proposed [23]. The deepened scales over the roughened wall keep breaking the boundary layers and promote the vorticity and turbulent activities. Local vortical cells are triggered when the flow traverses the protruding rims of scales either from the forward or backward direction. Taken into the account of increased cooling area by these deepened scales from the flat surface, this type of HTE mechanisms elevate the turbulent heat transfer in a non-rotating narrow channel to the levels about 3–4.5 times of Nu_∞ values for the backward and forward lows respectively [23]. In the past, considerable amounts of laboratory-scale heat transfer experiments using simplified models of the real blade cooling geometry with various HTE measures are well documented but only a few of these studies emulate the real engine conditions by operating the tests at high pressures [2,11,12]. The typical HTE effectiveness in terms of Nu/Nu_∞ ratio as exemplified in Fig. 1 falls about 2–2.5 and 2.5–4 over the stable and unstable walls respectively. The need to further elevate the HTE effectiveness above than those produced by the various HTE measures summarized in Fig. 1 with Ro range extended calls for the present study. The targeting data ranges for the present test channel roughened by the compound V-ribs and deepened scales are indicated in Fig. 1. This

series of rotating tests follows our previous work [27] in which the characteristics of heat transfer, pressure drop and thermal performances for the compound roughness of deepened scales and V-ribs in a rectangular channel with forward and downward flows were reported. But no previous study has examined the heat transfer performances for a rectangular channel roughened by such compound surface under the ***rotating*** conditions. This experimental study performs local heat transfer measurements along the centerlines of two roughened walls of a ***rotating*** rectangular channel with *Ro* and *Bu* considerably extended from the past experiences. The parametric analysis of heat transfer phenomena in association with the individual and interdependent effects of *Re*, *Ro* and *Bu* are illustrated along with the development of empirical heat transfer correlations. This set of heat transfer correlations accounts for the local heat transfer data generated by the present study that can uncouples the individual but mutually interdependent *Ro* and *Bu* effects on heat transfer.

2. Experimental details

2.1. Dimensionless parameters for heat transfer experiments

The technical community of experimental heat transfer for rotating channels has agreed that the Reynolds (*Re*) and rotation (*Ro*) numbers characterize the forced convection and the Coriolis forces in their own rights with the impacts of rotating buoyancy to be indexed by buoyancy number (*Bu*). The combination of density ratio ($\Delta\rho/\rho$) in terms of $\beta(T_w - T_b)$ with the relative centrifuge forms the non-dimensional group of $\beta(T_w - T_b)Ro^2(R/d)$ that is referred to as the buoyancy number (*Bu*) which physically reflects the relative strength of rotating buoyancy force. As a preliminary study to explore the heat transfer performances of the compound HTE measures using the deepened scales and V-ribs as an initial attempt, this experimental study examines the parametric variations of heat transfer performances in association with the relevant controlling dimensionless parameters. Variations of any governing dimensionless parameter such as *Re*, *Ro*, *Pr* or *Bu* for a set of pre-defined geometric and heating conditions result in different heat transfer performances. The heat transfer variation attributed from the systematic change of each of the governing flow parameters signifies the individual impacts of this varying parameter. Within the present tested T_b range of 302–326 K, the maximum variation in Prandtl number (*Pr*) of the tested coolant is negligible about 1.4%. Therefore the present parametric study is attempted to reveal the functional relationships between local Nusselt number (*Nu*) and the controlling dimensionless parameters in the form of

$$Nu = \Psi\{Re, Ro, Bu, X, \text{ geometric and thermal boundary conditions}\} \quad (1)$$

The unknown functional structure Ψ is to be discovered through this parametric study. The experimentally defined Nusselt number (*Nu*) is calculated as

$$Nu = qd/k(T_w - T_b) \quad (2)$$

In Eq. (2), the convective heat flux (q) is obtained by subtracting the external heat loss flux from the total heat flux supplied. It is noted that the additional heat transfer surfaces can be substantially acquired from the enhanced surfaces such as the pin-fin array, dimples or the ribs. In general, the heating area adopted for the dimpled and ribbed channels is often the projected area of the roughened floor so that such heat transfer data involves the additional fin effects from the extended surfaces [4,5,7,10,27]. But the fin effects of pin-fin array are not taken into account when the heat transfer coefficients are evaluated for the pin-fin channels using the adiabatic pin array [6,21,22]. As this study is attempted to compare the HTE effectiveness from the different HTE measures in the rotating channels available for cooling of rotor blades, the heating area adopted to evaluate the supplied and lost heat fluxes includes all the profiles of V-ribs and scales for the present compound surface. The area ratio between the total heat transfer surface of this compound roughness and the projected area of the roughened wall is 1.2. As a result, HTE ratios presented here for the non-rotating channel fitted with scales and V-ribs are 1/1.2 of those reported in [27].

A set of calibration heat loss tests is aimed at revealing the correlation between the external heat-loss flux and the wall-to-ambient temperature difference at the rotational speeds tested. The increase of rotational speed elevates the proportionality between the external heat-loss flux and the wall-to-ambient temperature difference. These heat loss proportionalities are correlated as the function of rotational speed that incorporates into the data processing program for evaluating the local heat loss flux. For this class of experiments, the maximum heat loss occurs at the test conditions with the highest rotational speed and wall temperatures, which is about 9% of the total heat flux supplied. Having defined the local convective heat flux (q) at each axial location where T_w is measured, the local enthalpy balance is accounted to determine the fluid bulk temperature (T_b) at the location where T_w is measured. All the fluid properties used to define the dimensionless parameters in Eq. (1) are then evaluated using these T_b values.

The approach for rig simulation of reducing mean flow velocity (W_m) with the coolant mass flow rate unchanged by raising the channel pressure extends *Ro* and *Bu* at any specified *Re*. Table 1 summarizes the present parametric range of experimental tests. It is noted that the maximum *Re* and *Ro* in Table 1 are not simultaneously attainable. Here the present ranges of *Ro* and *Bu* are considerably extended from the previous experiences [1–10,13].

2.2. Experimental program

This experimental study has three phases. Initially the static duct flow conditions are examined to generate the database against which the heat transfer results detected from the rotating channel are compared. Relative heat transfer enhancements from the Dittus–Boelter levels are determined and compared with the typical results collected from the static ribbed, dimpled and pin-fin channels. The second phase of study conducts a series of rotating experiments at the parametric conditions

Table 1
Range of dimensionless parameters

Dimensionless parameter	Range
Reynolds number [Re]	10000–24000
Rotation number [Ro]	0–2
Buoyancy number [$Bu = \beta(T_w - T_b)Ro^2(R/d)$]	0.004–7.9
Density ratio [$\beta(T_w - T_b)$]	0.06–0.27

Tested Reynolds numbers for each rotation number			
Ro	Re	Ro	Re
2, 1.5	10000	1.3	20000
1.4	15000	1, 0.8, 0.6, 0.5, 0.4, 0.3, 0.2, 0.1	10000, 15000, 20000, 24000

summarized in Table 1. Each set of rotating data generated in the second phase is produced at fixed Re and Ro by adjusting the rotational speed and the pressure level of test channel. At each selected Re–Ro combination, four ascending heater powers that raise the highest T_w levels to 353, 373, 393, and 403 K are supplied to reach four different steady state conditions. This measure adjusts the level of rotating buoyancy at fixed Re and Ro and generates a series of Nu data to reflect the isolated Bu effect on heat transfer. But such adjustments of heat flux vary fluid bulk temperatures that accordingly vary the fluid properties such as viscosity and thermal conductivity of the test coolant. In order to control Re and Ro at the flow entrance of test section within the maximum deviations of $\pm 1\%$ from the targeting values, the mass flow rates of test coolant are frequently adjusted to compensate the changes of fluid properties due to temperature variations.

The present study performs steady state heat transfer measurements. The steady state condition is assumed when the temporal wall temperature variations after several successive scans are less than $\pm 0.3\,^{\circ}\mathrm{C}$ after either the flow rate, rotational speed or the heating power is adjusted. Time intervals between such successive scans for checking the steady state are about 1 minute. Generally, the flow and heater power are kept for about 45 minutes in order to satisfy the steady state condition. All the relevant steady state measurements are processed into the dimensionless groups defined in Eq. (1) with the fluid properties determined from the local fluid bulk temperature.

In the second phase of data analysis, the isolation of buoyancy interaction from the Coriolis effects is not practical. This is because that the acquisitions of experimental heat transfer data require the finite wall-to-fluid temperature differences. As a result, the heat transfer data generated in the rotating test channel involves certain degrees of buoyancy impact. The separation of Re or Ro impact from Bu interaction is alternatively performed by extrapolating the rotational heat transfer data into the limiting condition of $Bu = 0$ while Re and Ro remain as the targeting test values. This regression process enables the determination of Nu data at the zero-buoyancy conditions so that the analysis of individual Re or/and Ro effects on heat transfer can be performed. Details in this regard will be further illustrated when the rotational Nu data is analyzed to generate the heat transfer data at the zero-buoyancy conditions.

The third phase of study analyzes and examines the heat transfer data generated in the first and second phases with the attempt to derive a set of heat transfer correlations for representing all the heat transfer data generated by this study. This set of heat transfer correlations also permits the evaluation of individual and interdependent effects of Re, Ro and Bu on local heat transfer along the centerlines of leading and trailing roughened walls in the periodically developed flow region. Along with the development of these heat transfer correlations, the dimensionless data are analyzed to determine the individual and interdependent impacts of Re, Ro and Bu on Nu in the rotating test channel. Typical heat transfer performances of rotating roughened channels are also compared with the present test channel to reveal the different rotational effects on heat transfer for the rotating surface with compound V-ribs and deepened scales.

The result of uncertainty analysis reveals that the most of the experimental uncertainties are attributed from the temperature measurements because the fluid properties are estimated from T_b. In general, the experimental uncertainties are improved for the tests with high heating powers and large Reynolds numbers. Applied the method of estimating experimental uncertainties recommended by the editorial board of ASME J. Heat Transfer [28], with the values of T_w–T_b in the range of 32–86 K, the estimated maximum uncertainties for Nu, Re, Ro and Bu are about 8.9, 7.6, 4.8 and 8.3%, respectively.

2.3. Rotating test rig and heat transfer test section

The rotating test rig has been designed to generate a rotating platform on which the assorted simulated blade cooling passage is mounted and tested. The constructional details of this rotating test rig along with its instrumentations for the measurements of flow-rate, heat-flux and temperature as well as the data acquisition system have been previously reported [11]. High pressure flow and heat transfer tests up to 8 bars are permissible so that the tested Ro ranges can be considerably extended. Test pressures of present study are controlled in the range of 1–2.6 bars to allow for the full coverage of the parametric conditions summarized in Table 1. With the present 450 mm long heat transfer test module mounted on the platform of the rotating rig, the midspan eccentricity (R) is 350 mm. The maximum t rotational speed of heat transfer test channel is up to 650 rev/min for this set of experiments. The test coolant flow (pressurized airflow) is supplied by two screw-type compressors from an air tank that is channeled through a set of pressure regulator and filter, a pressure transducer, a mass flow meter and a needle valve that controls the mass flow rate of airflow feeding into the heat

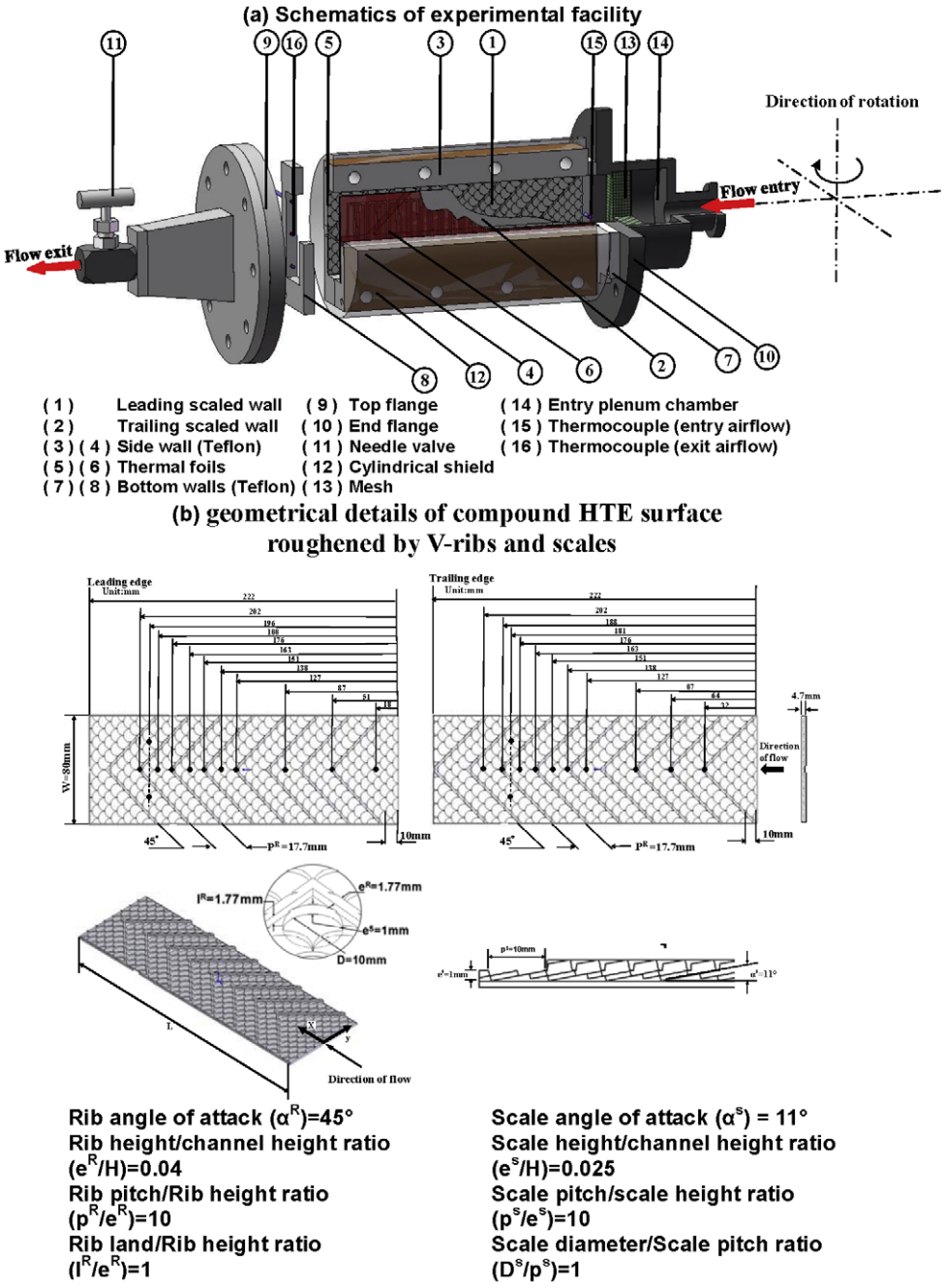

Fig. 2. Experimental apparatus (a) schematics of experimental facility (b) geometrical details of compound HTE surface roughened by V-ribs and scales.

transfer test module. Prior to entering the rotating test rig, the coolant is dehumidified and cooled to the ambient temperature.

Fig. 2 depicts the heat transfer test section that shows the assembly of test module (1-a) and the geometrical details of the compound V-ribs and deepened scales (1-b). As shown in Fig. 2(a), the rectangular test channel is made up of leading (1) and trailing (2) heated walls, together with two adiabatic Tufnol sidewalls (3)(4). The leading or trailing roughened wall (1)(2) is made of the stainless steel plate of dimensions $80 \times 40 \times 240$ mm and electrically heated by a 0.5 mm thick Minco thermal foil (5)(6) sandwiched between the Tufnol bottom plates (7)(8) and the Tufnol sidewalls (3)(4). Two basically uniform heat flux heating surfaces are simulated over the roughened leading and trailing walls (1)(2). Each heating foil (5) or (6) gives the active heating length of 240 mm. Electrical heating powers for these heating foils are supplied via a Variac transformer with the total power consumption metered by a Wattmeter. At each *Re–Ro* test condition, the heating powers are constantly adjusted in order to reach the pre-set T_w levels and vary the relative strength of buoyancy level.

Two pairs of opposite roughened walls (1)(2) and smooth sidewalls (3)(4) are physically tightened together by means of a series of axial bolts to form the rectangular test channel with the hydraulic diameter (d) of 30 mm. The complete set of test section is secured between the end and top flanges (9)(10) by four draw-bolts. A needle valve (11) is fitted on the convergent

exit flow passage to adjust the pressure level inside the rotating channel. Air leakage from each jointed surface is prevented by means of a series of 'O' ring seals and high temperature sealants. A cylindrical shield (12) is fitted between the end and top flanges with thermally insulated fiber filled to minimize the external heat loss. The heat transfer test module is vertically mounted onto the rotating platform with the dynamic balance ensured.

In front of the roughened test section, several layers of fine mesh (13) are installed inside the entry plenum chamber (14). Such abrupt flow entrance for the rectangular with the abrupt area ratio of 3 triggers the simultaneous development of thermal and hydrodynamic boundary layers at the immediate flow entrance. The entry air temperature is measured by a type K thermocouple (15) penetrating into the entry plenum chamber. Fluid properties used to evaluate *Re* and *Ro* at the flow entrance is based on this measured air inlet temperatures. At the exit plane of the rotating rectangular channel, three type K thermocouples (16) are positioned along the midline at three different spanwise locations with equal interval as indicated in Fig. 1(a). The measured T_b value at the exit plane of the test channel is obtained by averaging these three temperature measurements (16). However, as described previously, the enthalpy balance is accounted in order to determine the local T_b values at the axial locations where T_w values are detected using the sequential integration method. Wall-to-fluid temperature differences for local *Nu* evaluations are based on the calculated T_b values. However, the calculated T_b value at the exit plane for each test condition is checked with the average of three actual measurements (16). Only the experimental raw data is accepted and stored if the differences between the evaluated and measured exit T_b values are less than $\pm 10\%$.

Fig. 2(b) reveals the geometrical details of the compound scaled roughness and V-ribs. V-ribs on two opposite leading and trailing heated walls are arranged in the staggered manner with the following geometrical definitions defined in Fig. 2(b):

Rib angle of attack, α^R, $= 45^\circ$
Rib height, e^R (1.77 mm)/channel height, H (40 mm) $=$ 0.04
Rib pitch, P^R (17.7 mm)/rib height, e^R (1.77 mm) $= 10$
Rib land, l^R (1.77 mm)/rib height, e^R (1.77 mm) $= 1$

Surface scales are deepened into each scale-roughened surface between two adjacent V-ribs. These scales are arranged in the staggered manner on each roughened wall as seen in Fig. 1(b) with the following dimensionless geometrical descriptions:

Scale angle of penetration (α^S) $= 11^\circ$
Scale height, e^S (1 mm)/channel height, H (40 mm) $=$ 0.025
Scale pitch, P^S (10 mm)/scale height, e^S(1 mm) $= 10$
Scale diameter, D^S (10 mm)/scale pitch, P^S(10 mm) $= 1$

The ratio of channel width to channel height (aspect ratio) is 2. As indicated in Fig. 2(b), 10 K-type thermocouples are installed on the back of each leading or trailing roughened surface along its centerline for wall-temperature measurements. Locations of these thermocouples for T_w measurements correspond to the rib and mid-rib spots. In the final rib pitch over the leading and trailing roughened walls, two additional thermocouples at the mid-pitch and mid-span locations are installed to examine the spanwise heat transfer variations at the stationary and rotating conditions. At each thermocouple junction on the heated wall, the ceramic cement is applied to secure its position. Thermocouple wires are taken out of the test assembly via the grooves machined on two Tufnol back walls. All the temperature measurements are monitored and stored in a PC through the Net-Daq Fluke Hydra 2640A data logger for the subsequent data processing. Wall temperature measurements are corrected into the base-line surface as indicated in Fig. 1(b) using the one-dimensional heat conduction equation. The prescribed local heat flux used to correct the wall temperatures to the locations on the solid–fluid interface is the convective heat flux (q) quoted in Eq. (2). The origin of streamwise (x) and spanwise (y) coordinates is selected at the middle span of the test-section entrance. The x-wise direction is in the radially outward direction with the coolant flow initially traverses the protruding rims of scales, which is referred to as the forward flow condition [23]. As our previous study [23] reveals that the forward flow offers the higher HTE ratios with the better thermal performance factor in the rectangular channel roughened by deepened scales, the forward flow configuration as well as the radially outward flow condition is adopted by the present study.

3. Results and discussion

3.1. Heat transfer measurements in static channel

Fig. 3(a) depicts the axial distributions of HTE effectiveness in terms of Nu_0/Nu_∞ along the centerlines of the roughened leading and trailing walls at $Re = 10000$ and 24000. In the test channel with zero rotation, each pair of Nu_0 measurements along two opposite leading and trailing centerlines does not exhibit significant differences but only reflect the minor differences between the rib and mid-rib locations due to the staggered arrangement of V-ribs on two opposite roughened walls. The axial heat transfer profiles along the leading or trailing centerline as shown in Fig. 3(a) follow a general trend of exponential decay toward the developed levels subject to minor zig-zag variations triggered by V-ribs. The abrupt entrance generates the developing flow region in the axial span about $0 < x/d < 1.58$ where the overall heat transfer levels decay exponentially in the axial direction. The so-called periodically developed flow region emerges after the flow traversing about five pairs of V-ribs. Between each rib pitch on the leading or trailing roughened wall, local heat transfer rates are promoted by the deepened scales when the coolant flow traverses these scales. Due to such scale-induced regional heat transfer elevations over the area between two successive ribs, the amplitudes of zig-zag oscillations in the developed flow region are moderated from the results obtained with the smooth floor between two successive ribs as reported in [14,15,18].

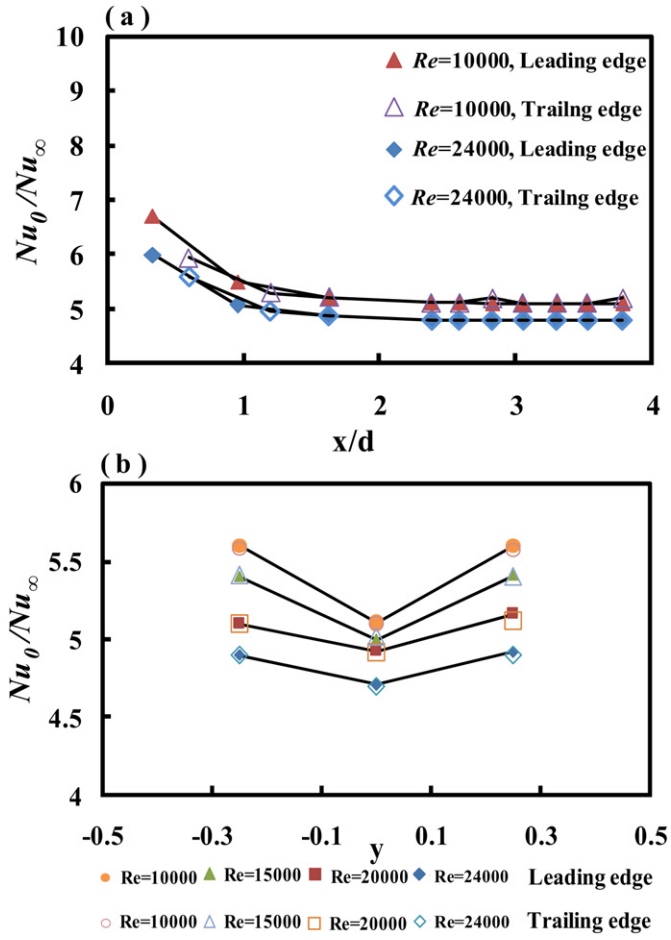

Fig. 3. Distributions of Nusselt number in static channel of (a) axial profiles with $Re = 10000$, 24000. (b) Rib-wise profiles with $Re = 10000$, 15000, 20000 and 24000.

Three sets of rib-wise heat transfer measurements along the mid-pitch centerlines in the periodically developed flow region of leading and trailing walls at $Re = 10000$, 15000, 20000 and 24000 are collected in Fig. 3(b) to indicate the rib-wise heat transfer variations in the static channel. As the V-ribs are pointed downstream, the rib-wise coolant stream flows from two edges of each roughened wall toward the mid-span apex of each V-rib. With the basically uniform heat flux condition, the wall temperatures increase in the rib-wise direction along the mid-rib centerline from two edges of each roughened wall toward the apex of V-rib. As a result, each Nu_0/Nu_∞ ratio at the central span location over leading or trailing wall is consistently lower than its two side counterparts along the mid-rib centerline (see Fig. 3(b)). The Nu_0/Nu_∞ ratios at the two side mid-rib locations share with the same levels at each Re tested over the leading or trailing wall as indicated in Fig. 3(b). Therefore the two pairs of rib-induced cross-stream vortices remain symmetrical in the static channel roughened by the present compound HTE surface.

In the test channel fitted with the compound roughness of deepened scales and V-ribs, the vortical cells are tripped by both scales and ribs. As the deepened scales are arranged in the staggered manner between two adjacent V-ribs, these scales are conjoint to form a large numbers of step-by-step protruding circular fronts that keep breaking the boundary layers over the roughened wall between each rib-pitch. Vortical flows tripped by scales promote vorticity and induce separated shear layers to augment turbulent activities. At the same time, the strong cross-stream secondary flows are tripped by the protruding V-ribs that sweep the highly turbulent vortical cells from these deepened scales toward the channel core for exchanges of heat/mass fluxes via furious fluid mixings. Such compound roughness has led to the broken boundary layers, enhancements of turbulence and vorticity, flow reattachments, small-scale vortical cells and the strong cross-stream secondary flows tripped by V-ribs that interact simultaneously to generate significant HTE effect. This is demonstrated in Fig. 3(a) by comparing the present heat transfer ratios (Nu_0/Nu_∞) with those obtained from the rib-roughened, dimpled and pin-fin channels [2,6,9,12,30]. While the HTE ratios found in the static rib-roughened, dimpled and pin-fin channels fall in the levels about 3, 2 and 2.2 times of Nu_∞ levels, the Nu_0/Nu_∞ ratios reach the range of 5.1–5.4 for the present test channel. However, as the heat transfer rates at the measurement locations on the present roughened walls may meet the regionally high spots, the Nu_0/Nu_∞ ratios can not represent the true average augmentation. It is also noticed that the various heat fluxes imposed to the static channel at each Re tested result in the similar Nu_0 values at each measurement spot so that the buoyancy effect on heat transfer in the present static channel is negligible.

The axial Nu_0 profiles reveal moderate zig-zag variations due to the presence of V-ribs and scales. The lower Nu_0 values at rib locations as shown in Fig. 3(a) are consistent with the experimental results detected from the thermocouple measurements such as those in [14] for which the surface ribs act as the thermal barriers for the heat flux from the heating foil to transfer into the flow. As it is impractical to correct the thermocouple measurements at rib locations to their rib-tops without the knowledge of convective heat transfer coefficients over all three faces of each V-rib, the representative heat transfer performances for the periodically developed flow are only examined at the mid-rib locations by this study. The three rib-wise heat transfer measurements at the final rib-pitch of the leading or trailing roughened wall are averaged as $\overline{Nu_0}$ and $\overline{Nu}$ for the static and rotating channels, respectively. The functional relationship between $\overline{Nu_0}$ and Re for the mid-rib performance is developed here. As the $\overline{Nu_0}$ values reflect the same flow features at the leading and trailing surfaces in the periodically developed flow region for the static channel, the $\overline{Nu_0}$ data at the mid-rib location is obtained by averaging the relevant Nu_0 data collected from the leading and trailing walls. Fig. 4 displays the varying manners of $\overline{Nu_0}$ versus Re. The Dittus–Boelter references over the tested Re range are also included in Fig. 4 for comparisons. The set of $\overline{Nu_0}$ data trend revealed in Fig. 4 is well correlated by Eq. (3) to feature the averaged mid-rib heat transfer performances in the periodically developed flow region of static channel at the forward flow condition.

$$\overline{Nu_0} = 0.165 \times Re^{0.771} \tag{3}$$

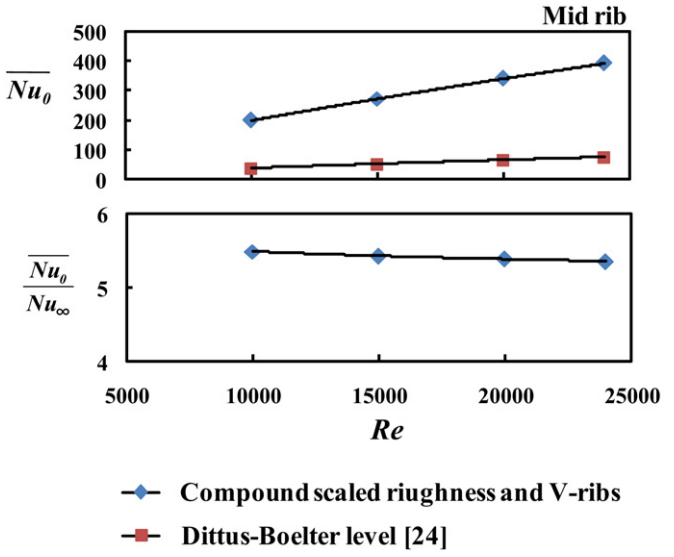

Fig. 4. Variations of rib-wise averaged Nusselt number in the periodically developed flow region against *Re*.

In the range of $10000 \leqslant Re \leqslant 24000$, all the present $\overline{Nu_0}$ measurements agree within ±3% discrepancies from the predictions of Eq. (3). It is noticed that the *Pr* effects are absorbed into the coefficient of Eq. (3), which are not included as a parametric effect when Eq. (3) is developed. Therefore Eq. (3) is essentially limited to dry air and used as the non-rotating heat transfer references to assess the influences of rotation on heat transfer. In this heat transfer correlation (Eq. (3)), the *Re* exponent of 0.771 is lower than but close to 0.8 in the Dittus–Boelter correlation. Hence the HTE effectiveness in terms of $\overline{Nu_0}/Nu_\infty$ ratio in the present test channel decreases as *Re* increases; but is a very weak function of *Re*. Therefore the *Re* range offering the effective HTE ratio is extended by using the present compound roughness.

3.2. General rotational heat transfer results

In the present test channel, the cross-stream Coriolis secondary flows can be generated throughout the entire rotating channel. Unlike the rotating pin-fin channel in which the Coriolis secondary flows can not be well established throughout the entire channel, the interactions of the vortical flows between Coriolis secondary flows and the vortices tripped by V-ribs and scales play a dominant role to signify the rotational effects on heat transfer. The Coriolis secondary flows convect the cooler fluids from the duct-core toward the trailing wall with the heated confluent flows jointed on the leading surface to preserve the mass continuity. This flow feature is referred to as the Coriolis washing effect that interacts with the vortices induced by V-ribs and scales to create the complex of vortical structures in the present rotating channel and result in peripheral heat transfer variations. In addition, the spanwise pressure gradients induced by Coriolis forces modify the local flow instabilities with the turbulences promoted and suppressed at the unstable (trialing) and stable (leading) surfaces, respectively. The flow instability phenomena along with the Coriolis

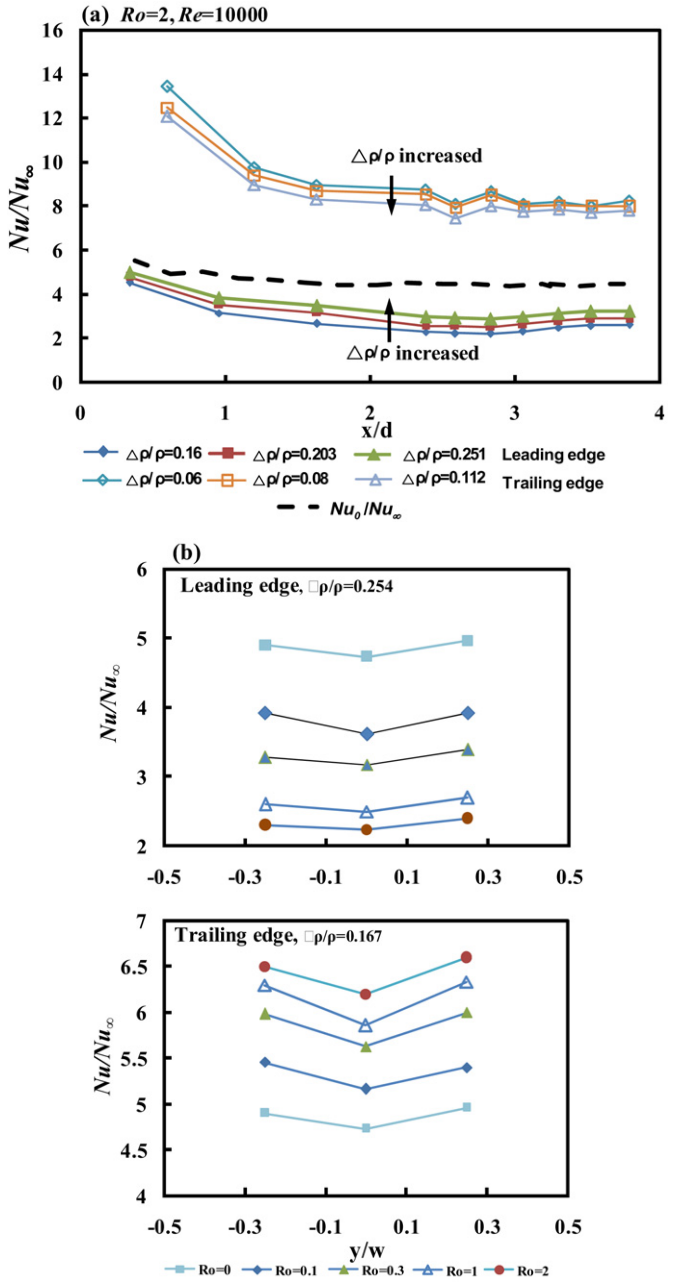

Fig. 5. Distributions of Nusselt number in rotating channel of (a) axial profiles with $Re = 10000$, $Ro = 2$. (b) Rib-wise profiles with $Re = 10000$, $Ro = 0$, 0.1, 0.3, 1, 2.

washing effect result in the higher *Nu* along the trailing centerline in comparison with its leading counterpart for all the rotating results. This is typified by Fig. 5(a) that displays the axial profiles of Nu/Nu_∞ ratio along the leading and trailing centerlines at $Re = 10000$ and $Ro = 2$. Unlike the Nu_0/Nu_∞ revealed in Fig. 4(a) with vanished buoyancy effect, the three sets of axial Nu/Nu_∞ profiles driven by three different heater power settings as shown in Fig. 5(a) demonstrate the noticeable buoyancy effects on heat transfer along leading and trailing centerlines. With all the parametric conditions examined, the respective heat transfer improvements and impediments from the zero-rotation reference along the trailing and leading center-

lines are consistently observed as typified in Fig. 5(a). But this *Re–Ro* combination is specifically selected to show the respectively improving and impeding *Bu* effects on heat transfer along the leading and trailing centerlines. As indicated in Fig. 5(a), the increase of $\Delta\rho/\rho$ ratios at the fixed *Ro* that incurs a corresponding increase of *Bu* produces the upward and downward data spreads at each axial station on the leading and trailing centerlines respectively. However, at the lower *Ro* values, the local Nu/Nu_∞ ratios at the leading edge also decrease with the increase of *Bu*. There is a critical *Ro* value above which the *Bu* effect turns from impeding to improving heat transfer along the leading centerline. Such so-called the reversal of buoyancy effect only develops at the leading edge within the present parametric conditions examined, while the *Bu* effects consistently impede local heat transfer along the trailing edge. Details in this respect will be presented in the later section that parametrically examines the isolated *Bu* effect on heat transfer.

It is also interesting to note the different degrees of heat transfer elevations (reductions) form the static Nu_0/Nu_∞ references between the developing and developed flow regions along the trailing (leading) centerline. The lager degrees of heat transfer elevations from the zero-rotation references along the trailing centerline are found in the developing flow region as shown in Fig. 5(a). The differences between Nu/Nu_∞ and Nu_0/Nu_∞ along the trailing centerline gradually decays in the axial direction into a "stable" condition at which the Coriolis secondary flows are maturely grown in the periodically developed flow region. But the converse of axial differences between Nu/Nu_∞ and Nu_0/Nu_∞ form the scenarios along the trailing centerline are observed along the leading centerline. Heat transfer impediments from the zero-rotation references increase in the downstream direction along the leading centerline that also lead to the "stable" condition in the periodically developed flow region. This particular heat transfer phenomenon for developing flows in this rotating channel requires the detailed flow measurements to clarify and is the result of interactions between the developing features of boundary layers, Coriolis secondary flows and the vortical cells tripped by V-ribs and scales.

The typical rib-wise heat transfer variations in the periodically developed flow region of the rotating channel are showed in Fig. 5(b). Although the rib-induced secondary flows are orthogonal to the Coriolis secondary flows over the cross-sectional plane of the present rotating channel, the pattern of rib-wise heat transfer variations over the leading or trailing surface follows those found in the static channel as indicated in Fig. 3(b). The symmetrically spanwise Nu_0/Nu_∞ variations as shown in Fig. 3(b) reflect the symmetrical secondary flow cells in respect to the leading or trailing centerline of the rotating channel. As *Ro* increases from 0.1 to 2, the systematic heat transfer elevations and impediments over the trailing and leading surfaces, respectively, are clearly demonstrated by Fig. 3(b).

Variations of heat transfer performances from the static conditions in the rotating channel are revealed by presenting the heat transfer results in terms of Nu/Nu_0 ratio. As Nu_0 is correlated as function or *Re* in Eq. (3), the convergence of different Nu/Nu_0 ratios obtained with different *Re* but at the same values of *Ro* and *Bu* indicates that the *Re* effect on *Nu* for the present rotating geometry follows that on the static heat transfer correlation for Nu_0. Such a case enables the isolation of *Re* impact from the influences of *Ro* and *Bu* on *Nu* by way of presenting the rotational heat transfer data in terms of Nu/Nu_0. This is testified by comparing several sets of Nu/Nu_0 data that are obtained with four tested Reynolds numbers but at a fixed *Ro* with the approximately same values of *Bu* along the leading and trailing centerlines as indicated in Fig. 6. As shown in each plot of Fig. 6 at the representative cases of $Ro = 0.1$, 0.3, 0.5, 0.8 and 1, four sets of axial Nu/Nu_0 profiles along the centerline of leading or trailing wall at $Re = 10000$, 15000, 20000 and 24000 collapse into a tight data band that demonstrates the feasibility of isolating *Re* impact from the rotational effects on heat transfer using Nu/Nu_0 data structure. As the *Re* impact on heat transfer performances in this rotating channel is isolated by presenting the rotational heat transfer data in terms of Nu/Nu_0, the data trends depicted in each plot of Fig. 6 reflect the combined effects of the streamwise development of *Ro–Bu* effect. The Nu/Nu_0 ratios along leading and trailing centerlines reach two asymptotic values in the periodically developed flow region with the higher ratios consistently developed at the trailing edge. Axial Nu/Nu_0 profiles along the leading and trailing edges still follow the non-rotational heat transfer data of exponential decay. The combined *Ro–Bu* impacts on local heat transfer along leading and trailing centerlines as exemplified by Fig. 6 are consistently observed for all the heat flux settings tested.

3.3. Parametric analysis of heat transfer results in rotating channel

Variations of heat transfer performances under rotating conditions from the non-rotating scenarios are parametrically examined here in view of the isolated and interdependent *Re*, *Bu* and *Ro* impacts on heat transfer. As described previously, the three rib-wise heat transfer measurements at the mid-rib locations within the final rib-pitch over the leading or trailing wall of the rotating channel are averaged as $\overline{Nu}$ to index the heat transfer level in the periodically developed flow region. The converged data points of $\overline{Nu}/\overline{Nu_0}$ ratios obtained with different *Re* but at the same values of *Ro* and *Bu* verify the isolation of *Re* impacts from the combined *Ro* and *Bu* effects by way of presenting the heat transfer data in terms of $\overline{Nu}/\overline{Nu_0}$. With the *Re* impacts isolated, the synergetic *Ro–Bu* impacts on heat transfer are able to be examined. In this respect, the *Bu* effect on heat transfer is initially examined by plotting $\overline{Nu}/\overline{Nu_0}$ ratios against *Bu* for the leading and trailing walls. Each plot in Fig. 7 displays the variations of $\overline{Nu}/\overline{Nu_0}$ ratios collected from all the *Re* tested at $Ro = 0.1$, 0.3, 0.5, 1, 1.5 and 2 against *Bu*. At the mid-rib location of the periodically developed flow region over the trailing wall, each *Ro* controlled data series as shown in Fig. 7(b) descends linearly as *Bu* increases. The isolated *Bu* effect impairs heat transfer on trailing wall. But the magnitude of the slope for each *Ro* controlled data series as shown in Fig. 7(b) systematically decreases as *Ro* increases with the tendency to turn from the negative to positive value. Although the general data trends shown in Fig. 7(b) for the trailing wall

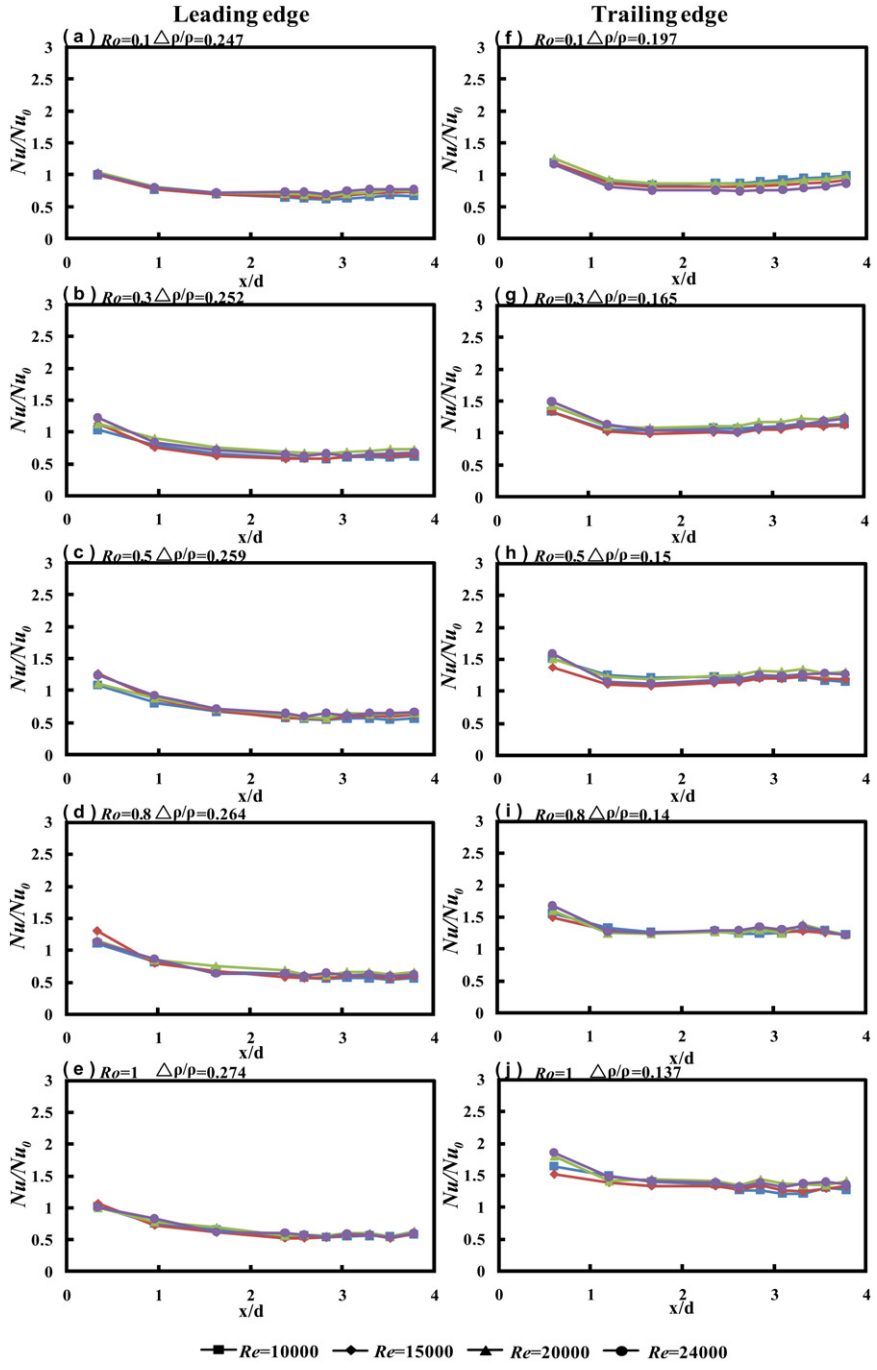

Fig. 6. Axial profiles of Nu/Nu_0 ratio at various *Re* with fixed *Ro* and density ratio.

are followed by those collected from the leading wall as seen in Fig. 7(a), the descending data series turns to the ascending data trend when *Ro* is increased above than 1. At such high *Ro* values ($Ro \geqslant 1$), the reversal of *Bu* effect from impeding to improving heat transfer develops on the leading wall. The variations of descending (ascending) rates of these *Ro* controlled data series showed in Fig. 7 (a) and (b) clearly demonstrate that the *Bu* effect on heat transfer is *Ro* dependent. Interdependent influences between the flow physics in association with *Ro* and *Bu* that affect the heat transfer performances in this rotating channel are confirmed. To uncouple the *Bu* effects from the *Ro* controlled thermal physics becomes impractical from the direct heat transfer measurements as the finite wall-to-fluid temperature differences, and therefore the involvements of *Bu* effects, are inevitable if *Nu* is experimentally defined. In the attempt to reveal the individual *Ro* impact on heat transfer, it is meaningful to identify the so-called zero-buoyancy heat transfer data by extrapolating each *Ro* controlled data series as seen in each plot of Fig. 7 to the limiting condition of $Bu = 0$ with vanished buoyancy level using the regressive type analysis. This type of linear curve fitting routine for each *Ro* controlled data series with a finite *Ro* value leads to the generation of $\overline{Nu}/\overline{Nu_0}$ level corre-

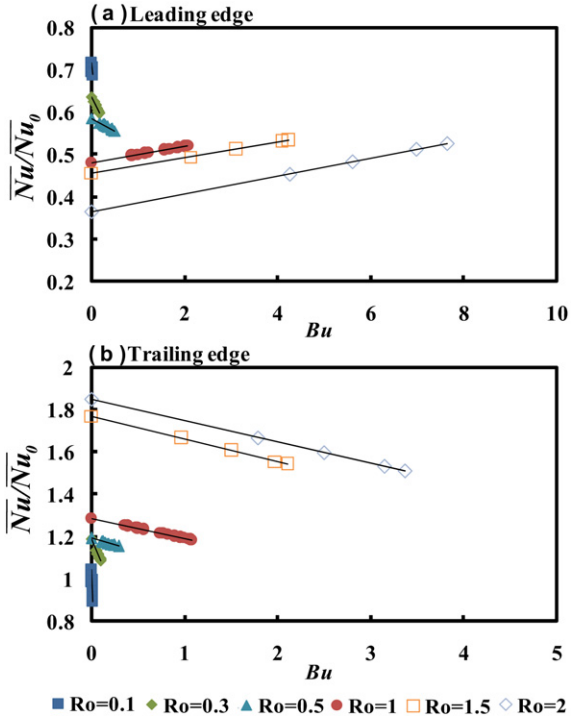

Fig. 7. Variations of $\overline{Nu}/\overline{Nu_0}$ against Bu at $Ro = 0.1$, 0.3, 0.5, 1, 1.5 and 2 (a) leading edge, (b) trailing edge.

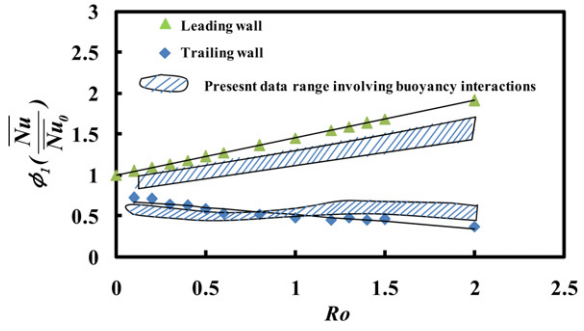

Fig. 8. Variations of ϕ_1 value in terms of $\overline{Nu}/\overline{Nu_0}$ ratio against Ro.

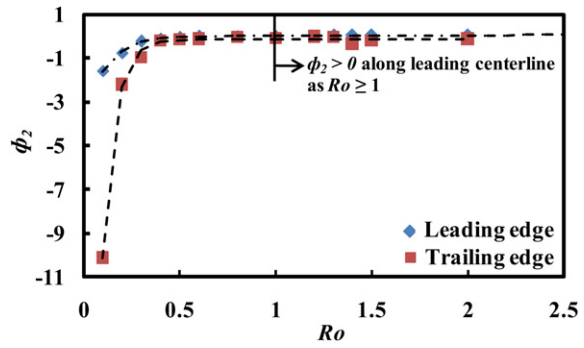

Fig. 9. Variations of ϕ_2 value in terms of $\overline{Nu}/\overline{Nu_0}$ ratio against Ro.

sponding to zero $\beta(T_w - T_b)$. Fig. 7 also shows the fitted lines for all the Ro controlled data series and the various $\overline{Nu}/\overline{Nu_0}$ ratios at zero-buoyancy conditions. These linear correlations as seen in Fig. 7 seem to fit well for all the Ro controlled data series so that the $\overline{Nu}/\overline{Nu_0}$ ratios over the leading and trailing walls of the rotating test channel are correlated by Eq. (4).

$$\frac{\overline{Nu}_{L,T}}{\overline{Nu_0}} = \phi_1\{Ro\} + \phi_2\{Ro\} \times Ro^2\beta(T_w - T_b)(R/d) \tag{4}$$

In Eq. (4), ϕ_1 and ϕ_2 are functions of Ro that are correlating functions for heat transfer results in the periodically developed flow region of this rotating channel. The ϕ_1 function evaluates the zero-buoyancy heat transfer levels that features the sole Coriolis force effects on heat transfer. The various slopes of the fitted lines as shown in Fig. 7 are taken into account by the ϕ_2 function that represents the various degrees of Bu impact on heat transfer. The negative or positive sign of ϕ_2 values respectively signify the impairing and improving heat transfer impacts while the magnitudes of ϕ_2 values reflect the degree of Bu impacts on heat transfer. Once again, the convergence of each Ro controlled data series obtained with different Re in all the plots of Fig. 7 reconfirms the applicability of scaling out Re effect from the combined Ro and Bu impacts on heat transfer by presenting the rotational heat transfer data in terms of $\overline{Nu}/\overline{Nu_0}$ ratio.

Fig. 8 depicts the variations of ϕ_1 value against Ro on the leading and trailing walls that reinstate the varying manners of the Ro controlled Coriolis force effects in isolation. Acting by the Coriolis force effect alone in the present rotating channel, the $\overline{Nu}/\overline{Nu_0}$ ratios on the leading wall tend to decrease linearly as Ro increases from 0.1 to 2. But the $\overline{Nu}/\overline{Nu_0}$ ratios increase in a form of complex exponential fashion as Ro increases on the trailing wall. However, the leading-wall heat transfer performances at the high rotation numbers ($Ro \geqslant 1$) can be somewhat elevated by adding the improving buoyancy effects as Bu effects turn from impairing to improving heat transfer at the high rotation numbers. The present data ranges with involvements of the impairing Bu effects on trailing wall and the impairing or improving Bu effects on leading wall are also included in Fig. 8. The ranges of $\overline{Nu}/\overline{Nu_0}$ ratios on the leading and trailing walls with involvements of Bu impacts are 0.7–0.5 and 1.1–1.6 respectively within the present parametric conditions examined. Converting the $\overline{Nu}/\overline{Nu_0}$ ratio into the HTE effectiveness in terms of $\overline{Nu}/Nu_\infty$ for two opposite rotating surfaces roughened by the present compound roughness, the $\overline{Nu}/Nu_\infty$ ratios on the leading and trailing walls respectively fall in the ranges of 2.7–3.3 and 5.7–8.8. The present type of rotating surface still offers the higher degrees of HTE ratios from those obtained in the rotating channels fitted with ribs, dimples or pin-fins. The lowest $\overline{Nu}/\overline{Nu_0}$ ratio or the so-called the worst heat transfer scenario for the present experimental conditions with the Bu effect involved develops at $Ro = 2$ with the minimum $\overline{Nu}/\overline{Nu_0}$ ratio of 0.5. The comparison of zero-buoyancy heat transfer levels between leading and trailing walls as shown in Fig. 8 reveals the increase of heat transfer differences between leading and trailing walls as Ro increases due to the growing strength of Coriolis secondary flows.

The variations of ϕ_2 versus Ro on the leading and trailing walls as shown in Fig. 9 are both followed by a general trend of complex exponentially fashion. Within the range of $0.1 \leqslant Ro \leqslant 2$, all the Ro controlled ϕ_2 functions remain negative on the trailing wall but reverse from negative to positive

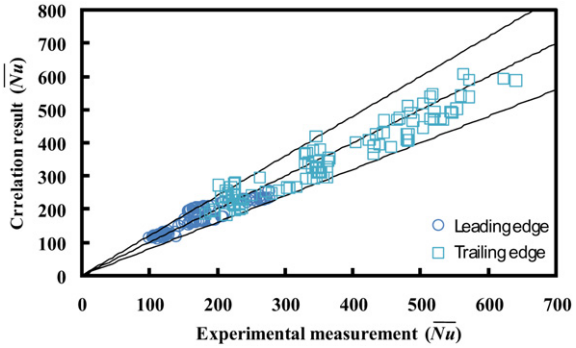

Fig. 10. Comparison of experimental measurements and correlation results in terms of $\overline{Nu}$.

on the leading wall. But the magnitude of the ϕ_2 function on the trailing wall is generally higher than that on the leading wall at each *Ro* examined. The trailing wall thus undergoes the more severe *Bu* impacts relative to its leading counterpart in the present rotating channel. Considering all the data trends revealed in Figs. 7–9, a set of heat transfer equations that evaluates $\overline{Nu}$ values at the mid-rib locations in the periodically developed flow region on the leading and trailing walls of the rotating channel is well correlated by Eqs. (5) and (6).

$$\overline{Nu} = (0.165 \times Re^{0.771}) \times \{[-0.175 + 0.691 \times Ro] + [0.0135 - 3.82\exp(-8.63 \times Ro) + 0.0213 \times Ro] \times Bu\} \quad (5)$$

$$\overline{Nu} = (0.165 \times Re^{0.771}) \times \{[1 + 0.34 \times Ro] + [-0.156 - 45\exp(-15.1 \times Ro) + 0.0146 \times Ro] \times Bu\} \quad (6)$$

Eqs. (5) and (6) have been derived following the present parametric analysis that resolve the uncoupled *Re* and interdependent *Ro–Bu* effects on *Nu* at the mid-rib locations in the periodically developed flow region of the present rotating channel. One of the purposes of deriving these heat transfer correlations is to represent all the heat transfer measurements produced by this study using these equations. Also the rotational $\overline{Nu}$ level can be evaluated by feeding the values of the controlling parameter such as *Re*, *Ro* and *Bu* into Eqs. (5) and (6). The comparison of all the experimental measurements with the correlative results for Eqs. (5) and (6) is performed to examine the success of these heat transfer correlations. There are 90% of experimental data found to be agreed with the correlation results within ±20% discrepancies. Fig. 10 shows such comparison between the experimental $\overline{Nu}$ data and the correlative results with the satisfactory agreements revealed. In view of the complicate and interdependent heat transfer physics in association with such compound HTE roughness, Coriolis forces and the rotating buoyancy, Eqs. (5) and (6) can be applied to approximate the heat transfer levels in the periodically developed flow region over the leading and trailing walls of the rotating channel. But the extrapolation of this set of heat transfer correlations beyond the parametric ranges specified in Table 1 gives rise to the uncertainties for evaluating $\overline{Nu}$ values. Justified by the higher levels of $\overline{Nu}/Nu_\infty$ ratios achieved by employing the compound HTE roughness of V-ribs and deepened scales in the rotating channel, this novel HTE surface is proved itself for potential applications to the cooling networks inside rotor blades.

4. Conclusions

The HTE performances for the novel compound roughness with V-ribs and deepened scales are testified under the rotating conditions with both ranges of *Ro* and *Bu* considerably extended into the realistic engine conditions. No previous study examines the heat transfer performances in the rotating channel fitted with the present compound HTE roughness. The following salient remarks are resolved by this study.

1. Without accounting for the fin effects from the extended surfaces of the V-ribs and deepened scales, the HTE effectiveness in terms of Nu_0/Nu_∞ for the present compound roughness falls in the range of 5.4–5.1 with $10000 \leqslant Re \leqslant 24000$ at the selected spanwise and centerline locations. The Nu_0/Nu_∞ ratio decreases with the increase of *Re* but is a weak function of *Re*. The $\overline{Nu_0}$ correlation that evaluates the averaged mid-rib heat transfer levels in the periodically developed flow region of the present static channel is derived.
2. The isolation of *Re* impact on rotational heat transfer from the interdependent *Ro–Bu* effects is achieved by representing the rotational heat transfer data in terms of Nu/Nu_0 or $\overline{Nu}/\overline{Nu_0}$. Due to the combined *Ro–Bu* impacts with the present parametric conditions, the $\overline{Nu}/\overline{Nu_0}$ ratios are in the ranges of 0.5–0.7 and 1.1–1.6 on the leading and trailing walls respectively. This is equivalent to the $\overline{Nu}/Nu_\infty$ ratios of about 2.7–3.3 and 5.7–8.8 at the detected spanwise and centerline locations.
3. The Coriolis force effect alone consistently reduces and increases $\overline{Nu}$ values on the leading and trailing walls, respectively, as *Ro* increases from 0.1 to 2. The worst heat transfer scenario develops on the leading wall that is mainly caused by the Coriolis effect and leads the ratio of $\overline{Nu}/\overline{Nu_0}$ ($\overline{Nu}/Nu_\infty$) to 0.4 (2.2).
4. The individual rotating buoyancy effect impairs heat transfer on the trailing wall but such *Bu* effect is reversed from impeding to improving heat transfer on the leading wall as *Ro* increases above than 1. The degrees of *Bu* impacts on heat transfer are generally weakened as *Ro* increases. Intercorrelative influences of *Ro* and *Bu* on heat transfer in this rotating channel are reconfirmed.
5. A set of heat transfer correlations that permits the evaluation of averaged Nusselt numbers at mid-rib locations of the periodically developed flow in the present rotating channel is derived to represent the experimental heat transfer data generated by this study with the individual and interdependent influences of *Re*, *Ro* and *Bu* on *Nu* to be assessed.

Acknowledgement

This research project was financially sponsored by National Science Council, Taiwan, under the grant number NSC 95-2221-E-022-018.

References

[1] M.E. Taslim, L.A. Bondi, D.M. Kercher, An experimental investigation of heat transfer in an orthogonally rotating channel roughened with 45 deg criss-cross ribs on two opposite walls, ASME J. Turbomachinery 113 (1991) 346–353.
[2] B.V. Johnson, J.H. Wagner, G.D. Steuber, F.C. Yeh, Heat transfer in rotating serpentine passages with trip skewed to the flow, ASME J. Turbomachinery 116 (1994) 113–123.
[3] S. Fann, W.-J. Yang, N. Zhang, Local heat transfer in a rotating serpentine passage with rib-roughened surface, Int. J. Heat Mass Transfer 37 (1994) 217–228.
[4] J.A. Parson, J.C. Han, Y.M. Zhang, Effects of model orientation and wall heating condition on local heat transfer in a rotating two-pass square channel with rib turbulators, Int. J. Heat Mass Transfer 38 (1995) 1151–1159.
[5] S. Dutta, J.C. Han, C.P. Lee, Local heat transfer in a rotating two-pass ribbed triangular duct with two model orientations, Int. J. Heat Mass Transfer 39 (1996) 707–715.
[6] F.T. Willett, A.E. Bergles, Heat transfer in rotating narrow rectangular pin-fin ducts, Experimental Thermal and Fluid Science 25 (2002) 573–582.
[7] L. Al-Hadhrami, J.C. Han, Effect of rotation on heat transfer in two-pass square channels with five different orientations of 45°angled rib turbulators, Int. J. Heat Mass Transfer 46 (2002) 653–669.
[8] T.-M. Liou, M.-Y. Chen, Y.-M. Wang, Heat transfer, fluid flow, and pressure measurements inside a rotating two-pass duct with detached 90-deg ribs, ASME J. Turbomachinery 125 (2003) 565–574.
[9] T.S. Griffith, L. Al-Hadhrami, J.C. Han, Heat transfer in rotating rectangular cooling channels (AR = 4) with dimples, ASME J. Turbomachinery 125 (2003) 555–563.
[10] S.W. Chang, W.D. Morris, Heat transfer in a radially square duct fitted with in-line transverse ribs, Int. J. Thermal Sci. 42 (2003) 267–282.
[11] S.W. Chang, T.L. Yang, W.J. Wang, Heat transfer in a rotating twin-pass trapezoidal-sectioned passage roughened by skewed ribs on two opposite walls, Heat Transfer Engrg. 27 (2006) 63–79.
[12] S.W. Chang, T.-M. Liou, W.-H. Yeh, J.-H. Hung, Heat transfer in a radially rotating square-sectioned duct with two opposite walls roughened by 45 degree staggered ribs at high rotation numbers, ASME J. Heat Transfer 129 (2007) 188–199.
[13] K.M. Kim, Y.Y. Kim, D.H. Lee, D.H. Rhee, H.H. Cho, Influence of duct aspect ratio on heat/mass transfer in coolant passages with rotation, Int. J. Heat Fluid Flow 28 (2007) 357–373.
[14] J.C. Han, Y.M. Zhang, C.P. Lee, Augmented heat transfer in square channels with parallel, crossed, and V-shaped angled ribs, ASME J. Turbomachinery 113 (1991) 590–597.
[15] M.E. Taslim, T. Li, D. Kercher, Experimental heat transfer and friction in channels roughened with angle, V-shaped, and discrete ribs on two opposite walls, ASME J. Turbomachinery 118 (1996) 20–28.
[16] H.H. Cho, S.J. Wu, H.J. Kwon, Local heat/mass transfer measurement in a rectangular duct with discrete ribs, ASME J. Turbomachinery 122 (2000) 579–586.
[17] X. Gao, B. Sundén, Heat transfer and pressure drop measurements in rib-roughened rectangular ducts, Experimental Thermal and Fluid Science 24 (2001) 25–34.
[18] X. Gao, B. Sundén, PIV measurement of the flow field in rectangular ducts with 60°parallel, crossed and V-shaped ribs, Experimental Thermal and Fluid Science 28 (2004) 639–653.
[19] G.I. Mahmood, M.L. Hill, D.L. Nelson, P.M. Ligrani, H.-K. Moon, B. Glezer, Local heat transfer and flow structure on and above a dimpled surface in channel, ASME J. Turbomachinery 123 (2001) 115–123.
[20] G.I. Mahmood, P.M. Ligrani, Heat transfer in a dimpled channel: Combined influences of aspect ratio, temperature ratio, Reynolds number, and flow structure, Int. J. Heat Mass Transfer 45 (2002) 2011–2020.
[21] M.K. Chyu, Y.C. Hsing, V. Natarajan, Convective heat transfer of cubic fin arrays in a narrow channel, ASME J. Turbomachinery 120 (1998) 362–367.
[22] S.Y. Won, G.I. Mahmood, P.M. Ligrani, Spatially-resolved heat transfer and flow structure in a rectangular channel with pin fins, Int. J. Heat Mass Transfer 47 (2004) 1731–1743.
[23] S.W. Chang, T.-M. Liou, M.H. Lu, Heat transfer of rectangular narrow channel with two opposite scale-roughened walls, Int. J. Heat Mass Transfer 48 (2005) 3921–3931.
[24] F.W. Dittus, L.M.K. Boelter, University of California, Publications in Engineering 2 (1930) 443.
[25] A.K. Viswanathan, D.K. Tafti, Detached eddy simulation of flow and heat transfer in fully developed rotating internal cooling channel with normal ribs, Int. J. Heat Fluid Flow 27 (2006) 351–370.
[26] S.W. Chang, W.D. Morris, A comparative study of heat transfer between rotating circular smooth-walled and square rib-roughened ducts with cooling application for gas turbine rotor blades, JSME Int. J. Ser. B 41 (1998) 302–315.
[27] S.W. Chang, K.F. Chiang, T.-M. Liou, G.F. Hong, Heat transfer and pressure drop in rectangular channel with compound roughness of V-shaped ribs and deepened scales, Int. J. Heat Mass Transfer 51 (2008) 457–468.
[28] JHT Editorial Board of ASME J. Heat Transfer, Journal of Heat Transfer Policy on reporting uncertainties in experimental measurements and results, ASME J. Heat Transfer 115 (1993) 5–6.
[29] J.H. Wagner, B.V. Johnson, T.J. Hajek, Heat transfer in rotating passages with smooth walls and radial outward flow, ASME J. Turbomachinery 116 (1994) 113–123.
[30] J.A. Parson, J.C. Han, Y.M. Zhang, Wall heating effect on local heat transfer in a rotating two-pass square channel with 90° rib turbulators, Int. J. Heat Mass Transfer 37 (1994) 1411–1420.